

Effect of Strain Rate on the Hot Ductility Behavior of a Continuously Cast Ti–Nb Microalloyed Steel

Marina Gontijo, Christian Hoflehner, Paul Estermann, Sergiu Ilie, Jakob Six, and Christof Sommitsch*

During the continuous casting process, alloys may be more susceptible to crack initiation under some conditions due to lower ductility. A Ti–Nb microalloyed steel is subjected to in situ melted hot tensile tests to evaluate its hot ductility behavior. The ductility is examined at different strain rates and temperatures. The samples are heated with an induction coil to the melting temperature in a vacuum atmosphere. Afterward, they are cooled to the desired test temperatures. Hot tensile tests are conducted by a thermomechanical simulator with strain rates varying from 10^{-5} to 10^{-2} s^{-1} . The results show a ductility minimum around $800 \text{ }^\circ\text{C}$ for the standard strain rate of 10^{-3} s^{-1} and a significant influence of the changes in strain rate in the behavior of the alloy for all the tested temperatures. The fracture surfaces are compared for 700 , 800 , and $900 \text{ }^\circ\text{C}$ at 10^{-4} , 10^{-3} , and 10^{-2} s^{-1} , as well as the microstructure. Computer simulations are done for the determination of the transformation temperatures, Scheil–Gulliver solidification simulation, and analysis of the precipitation kinetics during the tests. The results from simulations are discussed in comparison with the ones seen experimentally.

ductility curve presents a trough. This range is usually between 700 and $1000 \text{ }^\circ\text{C}$, depending on the chemical composition of the alloy.^[4–7] This loss in ductility can mainly be attributed to the austenite–ferrite transformation and the nucleation of precipitates.^[1,8,9] The ferrite forms films at the austenite grain boundaries, and as it has a lower strength than austenite, strain is accumulated making the material more prone to failure.^[6,9,10] Precipitates, when formed, provoke a local hardening, leading to stress concentration, that also worsens the ductility.^[1,11]

The evaluation of the hot ductility in steels is made with the reduction of area (RA), calculated from the relation between the initial cross-sectional area and the final, after the rupture of the sample.^[1–3] To evaluate the results, a reference value of 40% proposed by Mintz is used: when below this point, the ductility can be considered low and favorable to the formation of cracks.^[1,12]

The ductility of a steel grade can be influenced by diverse factors, such as the alloying elements, cooling rate, surface quality, strain rate, and others. This work evaluates the hot ductility behavior of a Ti–Nb microalloyed steel under variation of strain rate by performing hot tensile tests in in situ melted samples. The investigation focused not only on the ductility behavior, but also on the changes on the fractured surface, the microstructure, and precipitates. For the completeness of the evaluation, computer simulations were also performed for the transformation temperatures, Scheil–Gulliver solidification simulation, and precipitation kinetics.^[13]

1. Introduction

Many stress sources (mechanical and thermal) are present during the continuous casting process. These might lead to the initiation of cracks (at the surface or internal), which can cause premature failure of a steel slab.^[1–3] Therefore, avoiding or minimizing the formation of these cracks achieves better quality and lower costs to the process, which can be achieved with an improved hot ductility.

During the continuous casting process, the slab goes through a bending and straightening operation, which usually takes place at a critical temperature range for the material, where the hot

M. Gontijo, C. Hoflehner, Prof. C. Sommitsch
 Institute of Materials Science, Joining and Forming (IMAT)
 Graz University of Technology
 Kopernikusgasse 24/1, 8010 Graz, Austria
 E-mail: christof.sommitsch@tugraz.at

 The ORCID identification number(s) for the author(s) of this article can be found under <https://doi.org/10.1002/srin.202000222>.

© 2020 The Authors. Published by WILEY-VCH Verlag GmbH & Co. KGaA, Weinheim. This is an open access article under the terms of the Creative Commons Attribution-NonCommercial License, which permits use, distribution and reproduction in any medium, provided the original work is properly cited and is not used for commercial purposes.

DOI: 10.1002/srin.202000222

M. Gontijo, P. Estermann
 Area 2
 K1-MET GmbH
 Stahlstrasse 14, 4020 Linz, Austria

P. Estermann
 Institut für Werkstoffwissenschaft und Werkstofftechnologie (WWWT)
 TU Wien
 Getreidemarkt 9, 1060 Wien, Austria

Dr. S. Ilie, Dr. J. Six
 Department Research and Development
 voestalpine Stahl GmbH
 voestalpine-Strasse 1, 4020 Linz, Austria

2. Materials and Methods

2.1. Experimental

The microalloyed steel investigated has a chemical composition, as shown in **Table 1**. The samples were machined from a continuously cast slab into cylindrical dog-bone shape samples, with 15 mm of diameter and 160 mm of length, with their axis parallel to the casting direction.

The tensile tests were performed in a BETA 250-5 in-house built thermomechanical simulator, in a vacuum atmosphere (0.2 mbar). A Pt/Pt-Rh thermocouple was spot welded in the middle of the sample for the measurement of the surface temperature during the test. An induction coil is responsible for evenly heating the center of the specimen.

The temperature cycle used can be seen in previous studies.^[10,14,15] The samples were heated until the melting point, where the surface temperature was measured around 1450 °C, and held at this temperature for 90 s to ensure that the material was evenly heated until the center and the solution of all precipitates. Then, the sample was cooled, first at a rate of 5 °C s⁻¹ until 1250 °C, followed by a second rate of 1 °C s⁻¹ until the desired test temperature, which was held for 10 s before the start of straining. At first, the samples were tested at different temperatures, but with the same strain rate of 10⁻³ s⁻¹, which is the usual strain rate for the continuous casting process.^[1,8,10] Later, the tests were performed for three selected temperatures (700, 800, and 900 °C), with the strain rate varying from 10⁻⁵ to 10⁻² s⁻¹ until rupture of the specimen. After fracture, to evaluate the ductility, the reduction of area is calculated with the following equation:

$$\%RA = \left(\frac{A_0 - A_f}{A_0} \right) \times 100 \quad (1)$$

where RA is the reduction of area, A_0 is the initial cross-sectional area, and A_f is the fracture surface area, measured with the light optical microscopy (LOM).

Aiming on a more accurate value of A_0 , which leads to a more reliable result of RA, the diameter was investigated immediately before the start of the tensile test. For this purpose, the same initial steps of the temperature cycle were done (heating until melting and cooling until the test temperature), but the cycle was stopped before the beginning of straining. After complete cooling of the specimen, the diameter was measured and considered as the corrected initial diameter of the tensile test.

The fractured surfaces were documented with the aid of a scanning electron microscopy (SEM) for the comparison of the temperatures and strain rates. In addition, the microstructure of the tested samples was investigated with LOM and transmission electron microscopy (TEM). The samples were cut from the upper part of the specimen, approximately 1 mm away from the fracture surface. For the microstructure analysis with LOM, they were polished and etched with 3% Nital for the microstructure analysis with LOM.

Table 1. Chemical composition [wt%].

C	Cr	Mn	Al	Nb	N	Ni	P	S	Ti	Fe
0.081	0.037	1.43	0.041	0.046	0.0043	0.02	0.0096	0.0033	0.066	bal.

TEM investigations were conducted to characterize the precipitation state for the testing temperatures at 900 and 800 °C, both with the strain rate of 10⁻³ s⁻¹. At least seven energy-filtered transmission electron microscopy (EFTEM) images were done near the fracture surface of the tensile specimen, each covering an area of 800 × 800 nm and with a thickness of 50–100 nm. Electron energy loss spectroscopy (EELS) and energy-dispersive X-ray spectroscopy (EDX) spectrums were used to identify secondary NbTiCN and MnS precipitates. To analyze the particles found in the EFTEM images, the software Digital Micrograph, version 3.4.0, was used, with which the number density and mean radius of the particles could be determined.

2.2. Simulation

Thermodynamic databases and computational models were used with the software MatCalc (version 6.03.0117) in the thermokinetic simulations performed for the Ti–Nb microalloyed steel with the aim of predicting the precipitation behavior of MnS and NbTiCN. AlN was also considered in the first calculations and tested, but as this precipitate was not formed in a considerable amount to significantly affect the ductility (number density lower than 10⁸ m⁻³), it was not further investigated. NbTiCN nucleates at higher temperatures than AlN, consuming most of the N present, what makes it harder for AlN precipitates to form.

First, equilibrium calculations were made for the determination of the phase diagram. Scheil–Gulliver solidification simulations were then performed to predict the quantity of primary precipitates. Subsequently, thermokinetic simulations were performed for the different testing temperatures and strain rates to observe the nucleation of precipitates and the evolution of dislocations. The initial austenite grain size considered was of 500 μm, initial dislocation density of 10¹¹ m⁻², and a volumetric misfit of 5% between MnS precipitates at dislocations and the matrix.^[16,17] The 1-parameter Sherstnev–Lang–Kozeschnik (“ABC”) model is used to calculate the dislocation density and precipitation evolution of the evaluated steel, which is based on the one used by Kocks and Mecking.^[18] The time period considered for each tensile test and the ABC parameter used by the software in performing the simulations were adjusted on the basis of the experimental results.

The simulations of mean radius and number density were done at two selected temperatures, 900 and 800 °C. At lower temperatures, a considerable amount of ferrite is present simultaneously with austenite and this dynamic two-phase region cannot be precisely simulated. At 900 °C, there is still no indication of ferrite and although ferrite begins to form at a temperature slightly above 800 °C, the amount of this new phase at 800 °C is too small to significantly influence the behavior.^[14] The nucleation sites considered for NbTiCN were grain boundaries (gb) and dislocations (d) and for MnS, only dislocations.^[16,19–21]

3. Results

3.1. Experiments

The first evaluation of the alloy ductility was made at the usual continuous casting strain rate of 10⁻³ s⁻¹,^[1,8,10] at different

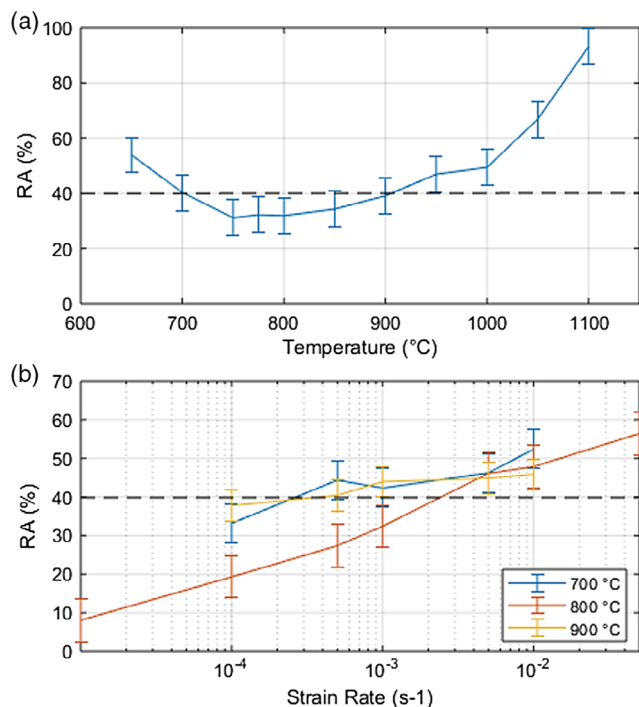


Figure 1. RA as a function of a) test temperature and b) strain rate.

temperatures, so that an overview of the hot ductility behavior could be obtained. At least two experiments have been conducted for each testing temperature. **Figure 1a** shows the resulted RA values as a function of the test temperature. The critical temperature range is where the hot ductility presents its lowest values, indicating that the material is more prone to failure in that region, which is referred to as the second ductility minimum. Taking the suggested reference value of 40% (indicated in the figure) into account, the range of poor ductility is observed from 700 to 900 °C. Between these values, the lowest part of the trough was between 750 and 850 °C, which makes these critical temperatures for the continuous casting process of the analyzed steel.

Above 900 °C and below 700 °C, an improvement in the ductility can be noted, which rises to RA values above the 40% line, indicating recovery of the ductility of the alloy.

Subsequently, fresh tests were made changing the strain rate at 700, 800, and 900 °C to evaluate how this change affects the hot ductility. These three temperatures were selected because they represent the critical temperature range for this steel. **Figure 1b** shows the results.

It can be inferred from the curves that the increase in strain rate incites significant changes in RA for the three tested temperatures. At 800 °C, a stronger influence of the strain rate can be seen in the larger range of RA values; however, at all temperatures, a higher strain rate led to an increase in RA. The lower RA values at 800 °C match the ductility minimum seen and explained in **Figure 1a**.

A more accurate value for A_0 is achieved from the samples tested without the tensile test. The experiments show an average increase of 2% in the sample diameter for this material after the melting and cooling cycle. This means, there is an average

change of about the same percentage in the calculated reduction of area, making the results more realistic and reducing associated errors.

The surfaces of the fractured samples were examined with SEM for a comparison of the failure mechanism and an analysis of the structure. The images can be seen and compared in **Figure 2**, where the differences, both in area and structure, with the different temperatures and strain rates can be seen. First, it can be noted, as expected, that the cross-sectional areas change visually with the increase in strain rate and temperatures. It can also be noted that at 800 °C (**Figure 2b**) this change in area is more significant than at the other temperatures, which was also predicted previously. Second, the structure of the fractured surfaces also presents changes with different temperatures and strain rates.

The evolution of the structure accompanies the changes as mentioned with the curves earlier. Brittleness can be identified by intercrystalline fracture, observed by the clear presence of grains and grain surfaces, which are mainly observed at 800 °C for all the strain rates. Ductile fracture is characterized by tear ridges, microvoids, and dimples, which are more present at the samples at 900 °C (**Figure 2a**) and 700 °C (**Figure 2c**). At these temperatures, less well-defined grain structures can also be seen. Furthermore, at each of the three temperatures, with the increasing strain rate, less grain surfaces were observed at each temperature, and more ductile fracture elements could be identified.

After sample preparation, the microstructure was observed with LOM and exemplary resulting images can be seen in **Figure 3**. The sample shown was tested at 800 °C, 10^{-3} s^{-1} .

In **Figure 3a**, prior austenite grain boundaries and acicular ferrite can be identified. The second of these is characterized by randomly distributed needles, as seen in the image.^[22,23] The formation of this structure is stimulated by any method that increases the number density of nucleation sites in austenite grain boundaries, such as the straining imposed in this case.^[22] Furthermore, a clear presence of voids along grain boundary can already be seen in the coalescence process.

Figure 3b shows a detailed image of a primary NbTiCN precipitate. These are formed before the final solidification of the material, as can also be seen in the Scheil–Gulliver simulation. These are usually relatively large and can be a cause for crack formation and consequent failure.

TEM investigations resulted in the values presented on **Table 2** and the images from **Figure 4**. In **Table 2**, a comparison is done between the values of means radius and number density obtained from the simulation and the ones measured with TEM from the tested samples. **Figure 4** shows the results from the TEM analysis that assured the formation of NbTiCN. The confirmation of the presence of MnS in this microalloyed steel is seen by the EDX mapping from a SEM image in **Figure 5**. Secondary MnS precipitates were not found, but the images showed cementite particles with a size ranging from 30 to 250 nm. It was not possible to measure the dislocation density with the TEM measurements.

3.2. Simulations

Equilibrium calculations resulted in the phase diagram are presented on **Figure 6a**. The results give information on the

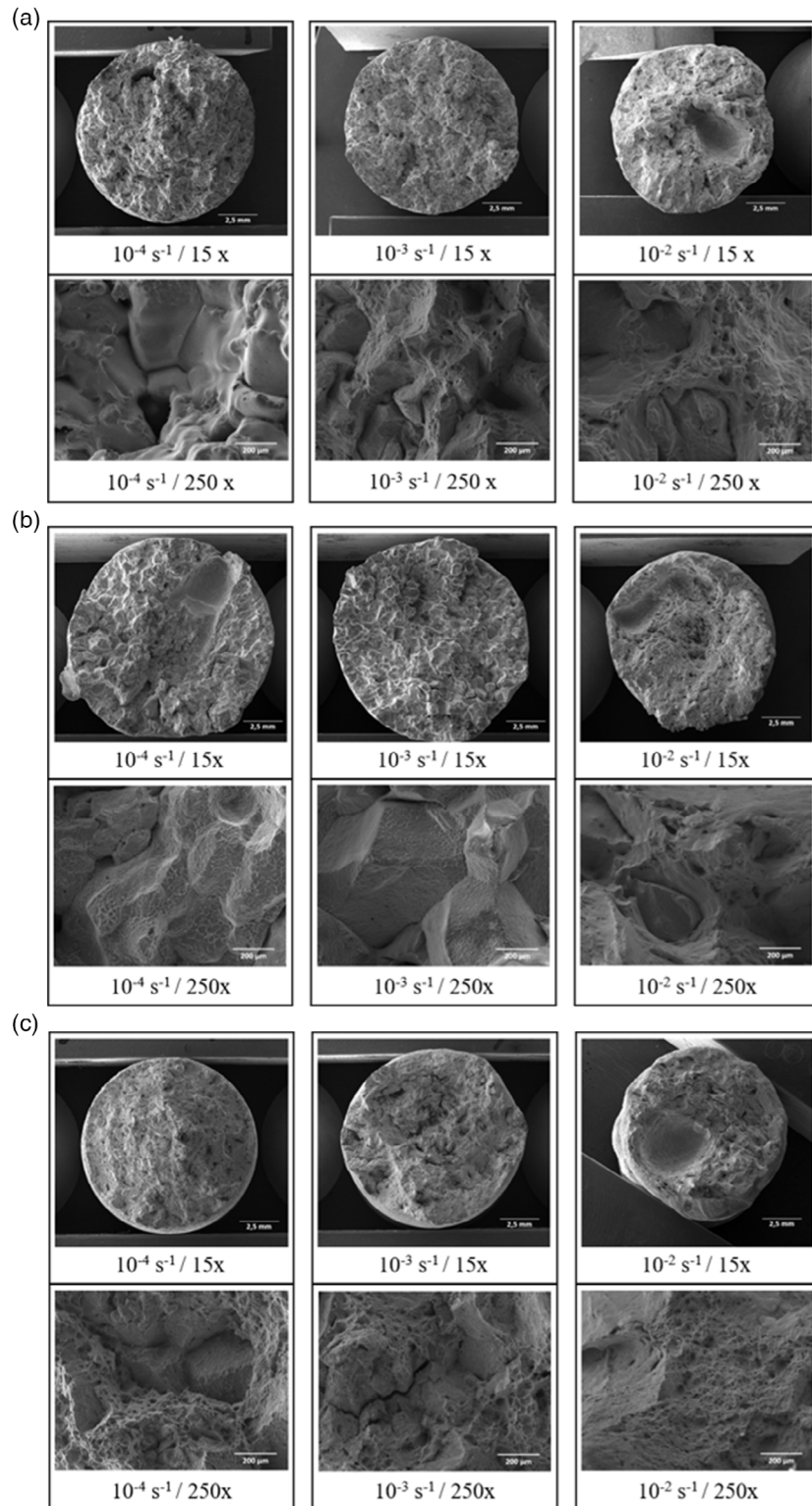


Figure 2. SEM images of fracture surfaces at a) 900 °C, b) 800 °C, and c) 700 °C.

transformation temperatures for each secondary phase as well as information on the predicted temperatures for the formation of secondary precipitates. Likewise, a Scheil–Gulliver simulation was performed for information on the formation of primary

phases during solidification considering very slow cooling (see Figure 6b).

The simulations for the precipitation kinetics were made at the selected temperatures (800 and 900 °C), at six different

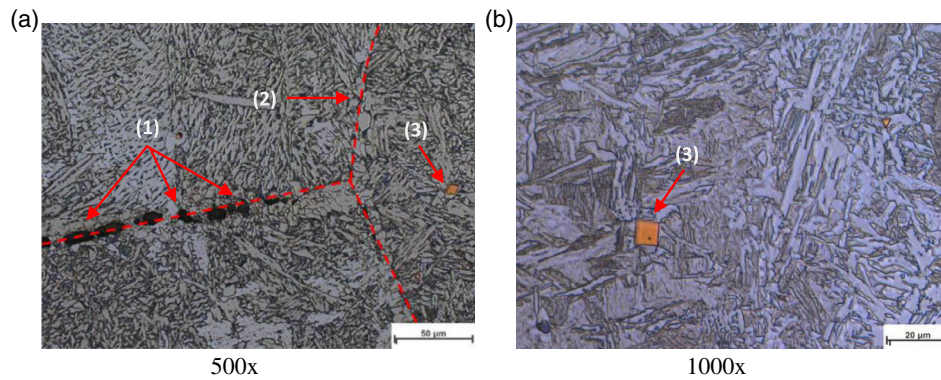


Figure 3. LOM images of microstructure after the tensile test at 800 °C, 10^{-3} s^{-1} , where voids 1) prior austenitic grain boundaries 2) and primary carbides 3) were identified.

Table 2. Results from simulations and experiments for NbTiCN(d) at 800 and 900 °C, at strain rates of 10^{-4} , 10^{-3} , and 10^{-2} s^{-1} .

	10^{-4} s^{-1}		10^{-3} s^{-1}				10^{-2} s^{-1}	
	800 °C	900 °C	800 °C		900 °C		800 °C	900 °C
	Simulated		Simulated	TEM	Simulated	TEM	Simulated	
Mean radius [nm]	5.37	8.03	2.00	2.45 ± 0.3	6.34	3.99 ± 0.74	0.73	2.06
Number density [m^{-3}]	$4.04 \text{ E} + 20$	$6.15 \text{ E} + 20$	$5.47 \text{ E} + 20$	$2.08 \text{ E} + 22 \pm 3.1 \text{ E} + 21$	$3.57 \text{ E} + 19$	$6.33 \text{ E} + 21 \pm 6.1 \text{ E} + 21$	$2.03 \text{ E} + 20$	$3.14 \text{ E} + 19$

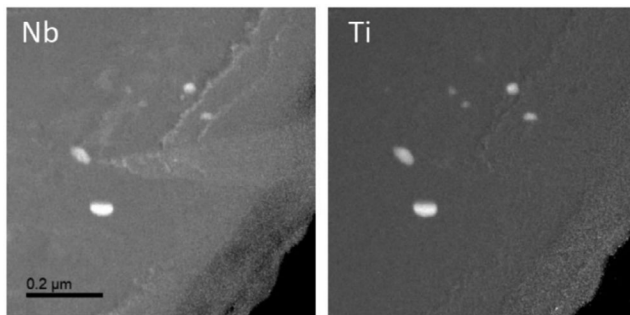


Figure 4. TEM analysis images of secondary NbTiCN precipitates from sample tested at 800 °C, 10^{-3} s^{-1} .

strain rates, from 10^{-5} to 10^{-2} s^{-1} . Based on results from the experiments, each tensile test was considered to have a different duration in accordance with the strain rate (longer for lower strain rates and shorter for higher strain rates). The mean radius and number density of NbTiCN and MnS were analyzed, together with the evolution of the dislocation densities.

The stress–strain curves resulting from the experiments were used to calibrate the aforementioned parameters of the model (ABC), taking the sample test length and the initial undeformed area into consideration, in accordance with the recent investigations of the initial cross section directly before the tensile test. Due to the way in which the software performs the calculations for this, the curves were shifted slightly to start at around 20–40 MPa to account for the elastic deformation.

The ABC model uses the following three parameters to scale the three mechanisms responsible for the evolution of the dislocation densities. The first parameter (A) is related to scaling

the dislocation generation of the precipitation domain during the deformation. The formula for the dislocation generation includes the Taylor factor, strain rate, the square root of the dislocation density, and Burgers vector, which represents the magnitude and direction of dislocation. A higher value for this parameter decreases the number of dislocations generated.

For determination of the second parameter (B), the dynamic recovery term is similar, and it depends on the Taylor factor, strain rate, annihilation distance, dislocation density, and Burgers vector. With an increase in this factor, the rate at which opposing dislocations cancel each other when the material is strained is also increased.

The third influence factor on the dislocation evolution to be considered is the static recovery, which depends on the factor C. Static recovery occurs because of the dislocation climb, and apart from factor C, it is also dependent on the effective diffusion coefficient, the shear modulus, Burgers vector, dislocation density, and equilibrium dislocation density. All these factors are in relation with the Boltzmann constant and the temperature. Of all the three presented factors, this one is the most influenced by the temperature.

By comparing the results of the strength simulation with the measurements of the experiments, the values of these parameters are tweaked for a better fit to the experiments. The values $A = 36$, $B = 15$, and $C = 0.015 \times \epsilon^{0.7}$ were found to represent the steel used in this article. It must be noted that variations in the experimental results together with the thermodynamic database and the program version used for the simulations can have a considerable impact on the results.

Figure 7 shows the mean radius and number density results for the secondary precipitates formed at dislocations and grain boundaries at 800 °C (Figure 7a) and 900 °C (Figure 7b). At both

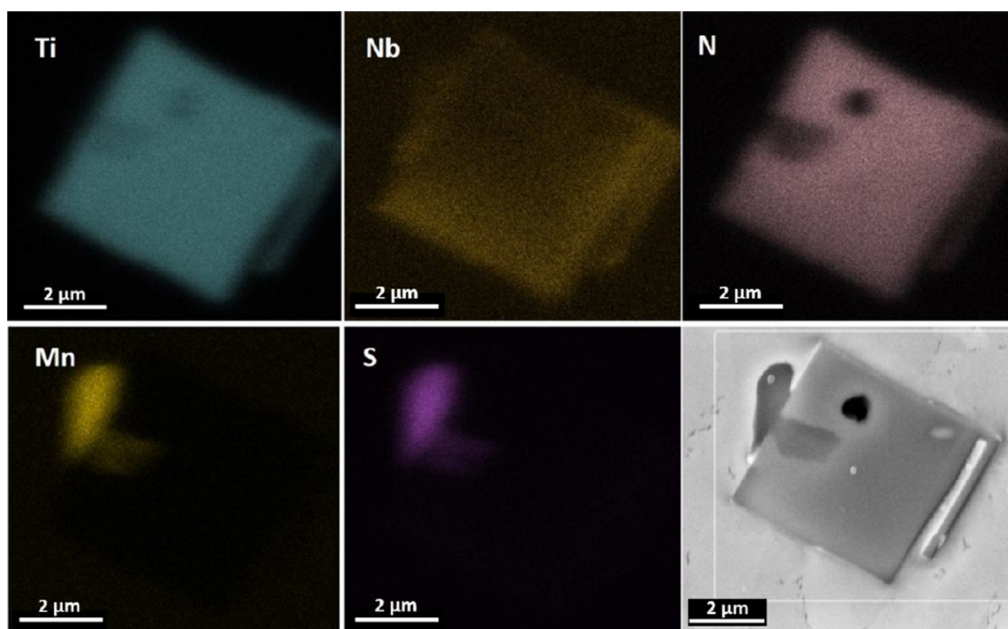


Figure 5. SEM–EDX mapping of primary NbTiCN and MnS from a sample tested at 800 °C and 10^{-3} s^{-1} .

simulated testing temperatures (800 and 900 °C), the size of precipitates at dislocations was seen to reduce with increasing strain rate. On comparing the results, at 800 °C the precipitates at these sites were found to be smaller than at 900 °C. For the precipitates formed at grain boundaries, no significant variation in the results of mean radius was seen.

In the context of the number density, the simulations showed a change in behavior at both temperatures at around 10^{-3} s^{-1} for precipitates at dislocations. From the lower simulated strain rate until the critical point of 10^{-3} s^{-1} , there was an increase in number density, followed by a decrease, indicating less nucleation. Again, at 800 °C, there is a general difference and the resulting values were one order of magnitude higher than at 900 °C.

The results for NbTiCN formed at grain boundaries are not shown because the values obtained for the simulations of mean radius (215 nm) and number density ($8 \times 10^{10} \text{ m}^{-3}$) were constant in both testing temperatures and all strain rates. MnS was not simulated at grain boundaries because at lower temperatures, as the ones chosen for the simulations, it nucleates preferably at dislocations.

Dislocation density was likewise simulated with the same software and parameters, and the results showed an increase in dislocation density with increasing strain rate, which can be seen in **Figure 8**. Resulted values were higher for 800 °C when compared with 900 °C.

4. Discussion

4.1. Experimental

The addition of Ti and Nb was previously seen to be detrimental to the ductility, even though a finer microstructure can be observed.^[2] This lower ductility, and specially the ductility minimum observed in **Figure 1a**, is mainly associated with two

phenomena, which are the formation of precipitates and ferrite films at austenite grain boundaries.^[1,2,6,7,9,10] The occurrence of both is not only influenced by the temperature, but also by the deformation applied. Some of the ferrite present in the material is induced by deformation during the tensile test and is responsible for the ductility trough.^[12,20] In addition, more dislocations are formed when the material is strained, which results in sites for the nucleation of precipitates. Together with ferrite and precipitates, the formation of voids is also detrimental to the ductility because these can coalesce and begin to form microcracks. The occurrence of the three phenomena (ferrite films, precipitates, and voids) is validated with the SEM and LOM images shown in **Figure 2** and **3**. In **Figure 3a**, the voids seen at the grain boundaries, showing signs of coalescence, are highly detrimental to ductility, in addition to the primary precipitates.

The better ductility at above 900 °C is associated with the absence of ferrite, being the behavior governed by austenite, as well as less dislocations (at higher temperatures there is lower dislocation density due to annihilation). The improvement in RA below 700 °C is caused by a greater amount of ferrite in the material, surpassing the critical ratio between austenite and ferrite. Ductility was seen to be at a minimum when the ferrite amount is around 5–10% and then to recover when this fraction is increased to around 50%.^[6] With more ferrite, no concentration of strain occurs in thin ferrite films at the grain boundaries, thus avoiding the formation of cracks in these regions. The minimization of strain in grain boundaries enables the material to withstand more plastic strain, improving the ductility.^[1,6] Furthermore, at a higher fraction of ferrite, there is more dynamic recovery, reducing the number of dislocations in the matrix.^[1]

The improvement in RA seen with the increase in strain rate (**Figure 1b**) is in accordance with a number of published results.^[1,5–7] This enhancement can be related to the different

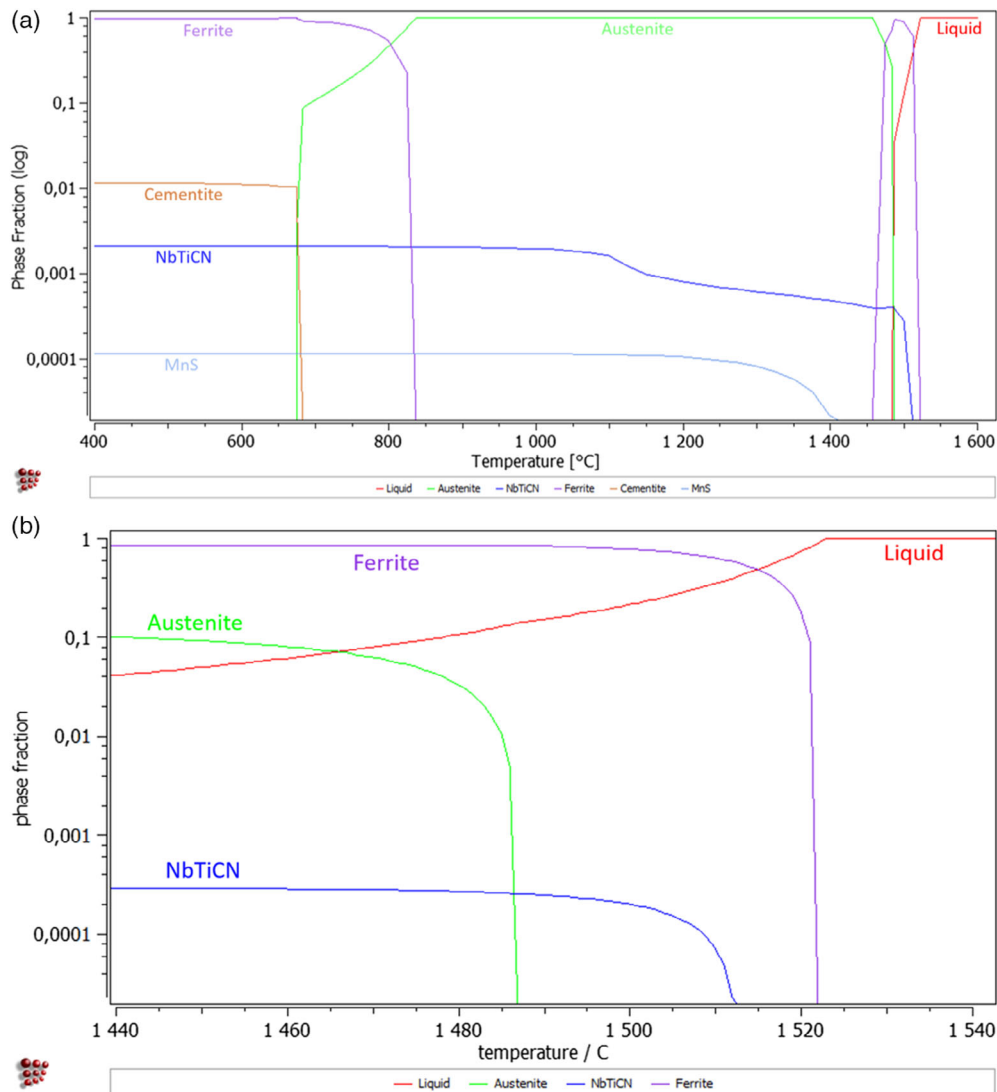


Figure 6. Equilibrium calculations a) phase diagram and b) Scheil–Gulliver simulation.

time duration of the tests because the samples rupture sooner when strained at higher strain rates. Thus, there is less time available for the formation of deformation-induced ferrite and the nucleation of precipitates when the strain rate is increased. Furthermore, work hardening occurs in the ferrite that is formed at higher strain rates with the strength achieved approximating that of austenite, which makes it less prone to failure.^[1,7,8] In addition to these factors, the void fraction is reduced with a higher strain rate because of the reduced time for its nucleation.^[24,25]

Information on the fracture could be obtained from the images made with SEM (Figure 2). More changes in the structure with increase in the strain rate could be seen at 800 °C, which are related to the lower ductility at this temperature, and this is also borne out by the curve in Figure 1b. The lower ductility at this temperature is attributed to the presence of deformation-induced ferrite films in austenite grain boundaries. This can be confirmed in the images from Figure 2b, where the grains

are larger and ferrite can be seen in their surfaces. The improvement of ductility with an increasing strain rate in these figures can also be clearly seen with the evolution of grain size and the clear reduction in number of distinct grain surfaces. There was also more indication of ductile fracture at the highest strain rate, mixed with less identifiable grains, indicating the improvement of ductility, as expected from the RA results.

At 900 and 700 °C, the structure seen (Figure 2a,c) is also in accordance with the results from Figure 1 because there is a clear majority of ductile fracture areas instead of grain surfaces, with dimples, microvoids, cleavage, and tear ridges. At 900 °C, this type of fracture and better ductility are due to the absence of a significant amount of ferrite being formed, as mentioned earlier, which cannot be seen or confirmed in the SEM images. Furthermore, the improvement at the lower temperature (700 °C) is caused by the opposite behavior also as stated, with a greater amount of ferrite present. This structure can be seen at the grain surfaces in the images from Figure 2.

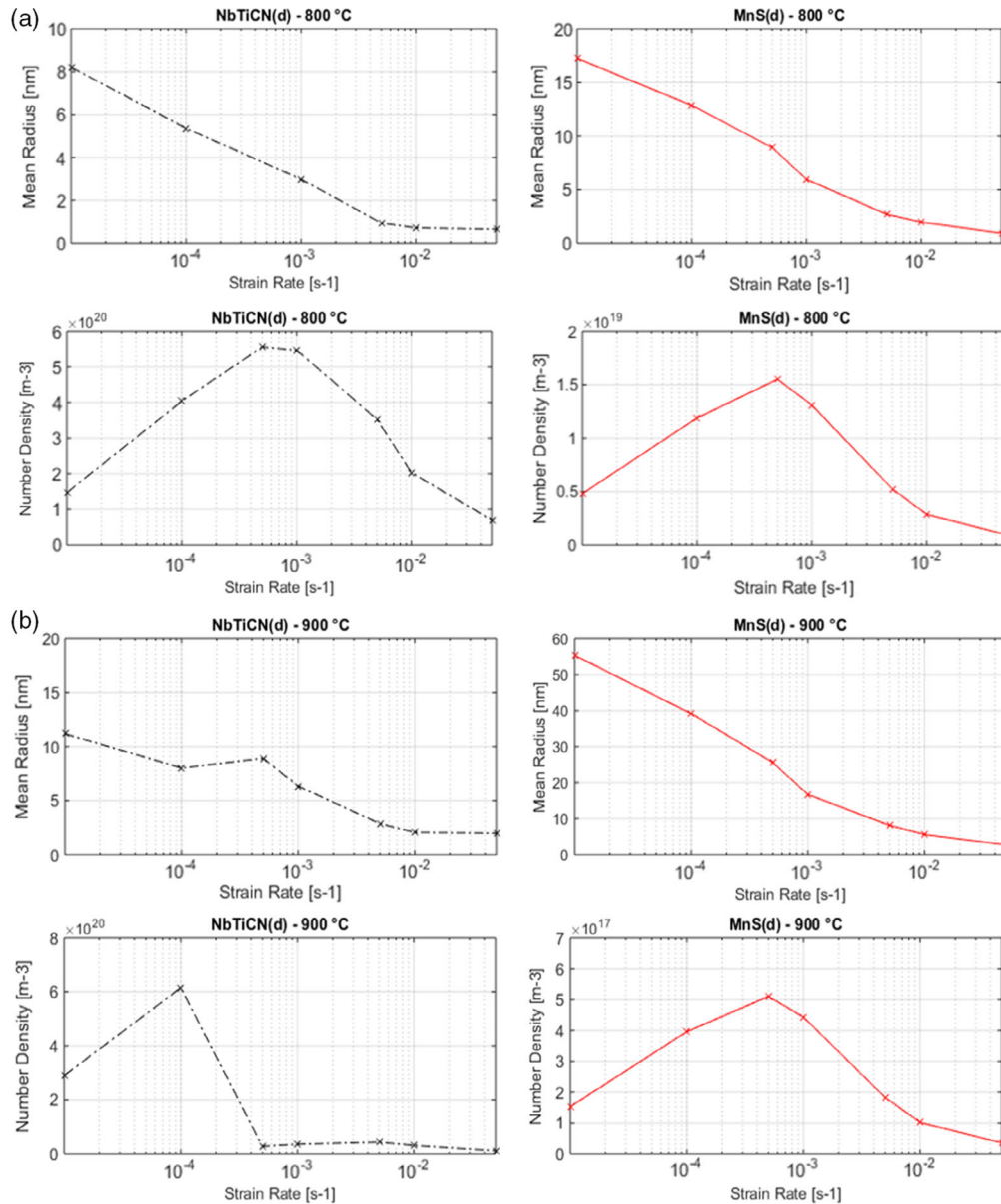


Figure 7. Simulated mean radius [nm] and number density [m^{-3}] of MnS and NbTiCN precipitates at dislocations as a function of strain rate at a) 800 °C and b) 900 °C.

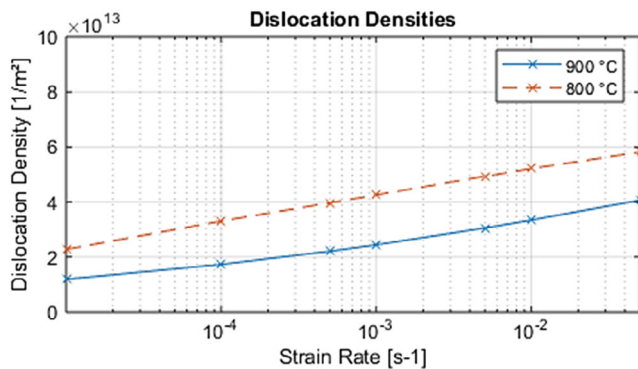


Figure 8. Simulated dislocation densities at 800 and 900 °C.

4.2. Simulation

From the results of the mean radius simulation, a reduction is seen with the increase in strain rate. This is caused by the shorter test durations resulting in less time for the precipitates to grow. The smaller results at 800 °C compared with 900 °C are due to the lower growth rate, consequence of less diffusion at lower temperatures. These results can be related to those seen experimentally, in the sense that finer precipitates impair the ductility.^[1,3,5,9]

The results seen for the number density above 10^{-3} s^{-1} can also be explained by the test duration, when there is less time for the nucleation of the precipitates at higher strain rates. This is also a reason for the improvement seen in hot ductility

with the increase in the strain rates because precipitates have a harmful effect on ductility. The lower number density at 900 °C in comparison with 800 °C is due to the greater coarsening of precipitates at higher temperatures. This is in conformity to the mean radius results, which also reflect the experimental results (lower ductility at 800 °C), once precipitates are more unfavorable when finer and in higher quantities.

The simulation of dislocation density shows good agreement with the theory, as the plateau during deformation reaches higher values for higher deformation rates and lower temperatures. The lower density for the higher temperature (900 °C) is due to the occurrence of more annihilation of dislocations at greater temperatures. This is also a result that matches with the behavior seen in the experimental work. Higher dislocation density means more sites for the nucleation of precipitates, and with a consequent decrease in the ductility. The lower values seen at 700 °C are explained by the large quantity of ferrite present having better dynamic recovery properties under deformation than austenite.^[1,18,24]

At lower strain rates, however, a lower dislocation density was seen, but also lower RA values. This indicates that the phenomena simulated (mean radius, number density, and dislocation density) have a weaker effect on the hot ductility behavior of the material. The fact of the matter is that below 10^{-3} s^{-1} what decreases the ductility is the formation and coalescence of microvoids, which are influenced by the strain rate, formed in a greater quantity when the strain rate is lower, because there is more time for their nucleation, impairing the ductility at these points.^[24,25] Above the critical strain rate of 10^{-3} s^{-1} , both the dislocation density increases and the RA values. In this case, even though there are a greater number of dislocations, there is not enough test time for the precipitates and microvoids to nucleate and coalesce at these new dislocations, as seen with the reduction of number density of precipitates and less voids to be seen in the images from the SEM analysis.

TEM analysis showed that the mean radius simulations are in good accordance with the experimental results, but that does not stand for the number density. The simulations underestimate the number density of the precipitates compared with the TEM measurement. In addition, the images proved the formation of primary and secondary NbTiCN precipitates, as well as MnS.

5. Conclusions

The second ductility minimum for the strain rate of 10^{-3} s^{-1} is between 750 and 850 °C, caused by the presence of deformation induced ferrite films at austenite grain boundaries, precipitates, and voids. The presence of these three factors was confirmed by LOM, SEM, and TEM analysis. Above 850 °C the improvement in ductility is due to less ferrite and annihilation of dislocations at higher temperatures. Below 750 °C the larger amount of ferrite, surpassing the critical ratio, is the reason for the improvement.

Changes on strain rate strongly influence the ductility behavior of the material. With higher strain rates, the alloy has better ductility at all temperatures, with enhanced results at 800 °C. This improvement at higher rates is directly connected to the different test durations at the varied strain rates. With a shorter test

time, there is less time for the formation of deformation induced ferrite, ferrite work hardening and nucleation of voids.

Simulations showed the same trend of behavior when compared to experimental results. Finer precipitates with higher number density at 800 °C are in accordance with the lower ductility seen at this temperature. The lower dislocation density at 900 °C is a result of the greater annihilation that occurs at higher temperatures, improving the ductility.

The values of the simulated mean radius of the precipitates are in good agreement with the TEM measurements, but the number density is underestimated by the simulation when compared to the measurements. At lower strain rates (below 10^{-3} s^{-1}), the nucleation and coalescence of voids are the driving factor for the worsening of the ductility. Apparently, the mean radius and number density of precipitates, as well as the dislocation density, have a smaller influence on ductility.

A reduction of the Ti content could result in a significant reduction of NbTiCN precipitates and consequent improvement of ductility. However, the goal of this research was not to change the chemical composition, chosen to improve the mechanical properties at room temperature. Therefore, to improve the ductility it is suggested to consider increasing the casting speed, even if in small amount, to achieve a strain rate higher than 10^{-3} s^{-1} .

Acknowledgements

The authors gratefully acknowledge the funding support of K1-MET GmbH. The research program of the K1-MET competence center is supported by COMET (Competence Centre for Excellent Technologies), the Austrian program for competence centers. COMET is funded by the Federal Ministry for Climate Action, Environment, Energy, Mobility, Innovation and Technology, the Federal Ministry for Digital and Economic Affairs, the provinces of Upper Austria, Tyrol and Styria, and the Styrian Business Promotion Agency (SFG). In addition, this research project is partially financed by the industrial partners Primetals Technologies Austria and voestalpine Stahl and the scientific partners Graz University of Technology and TU Wien.

Conflict of Interest

The authors declare no conflict of interest.

Keywords

continuous casting, hot ductility, low alloyed, steels, strain rate

Received: April 23, 2020

Revised: June 25, 2020

Published online: July 26, 2020

- [1] B. Mintz, S. Yue, J. J. Jonas, *Int. Mater. Rev.* **1991**, *36*, 187.
- [2] M. M. Arikan, *Metals* **2015**, *5*, 986.
- [3] O. Caliskanoglu, *Doctorate Thesis*, Graz University of Technology, **2015**.
- [4] B. Mintz, D. N. Crowther, *Int. Mater. Rev.* **2010**, *55*, 168.
- [5] R. Abushosha, S. Ayyad, B. Mintz, *Mater. Sci. Technol.* **1998**, *14*, 227.
- [6] J. Lewis, J. J. Jonas, B. Mintz, *ISIJ Int.* **1998**, *38*, 300.
- [7] D. N. Crowther, Z. Mohamed, B. Mintz, *Trans. ISIJ* **1987**, *27*, 366.
- [8] B. Mintz, J. Lewis, J. J. Jonas, *Mater. Sci. Technol.* **1997**, *13*, 379.

- [9] K. M. Banks, A. Tuling, B. Mintz, *Mater. Sci. Technol.* **2012**, 28, 536.
- [10] C. Beal, O. Caliskanoglu, C. Sommitsch, S. Ilie, J. Six, M. Domankova. *Mater. Sci. Forum* **2016**, 879, 199.
- [11] B. Mintz, J. J. Jonas, *Mater. Sci. Technol.* **1994**, 10, 721.
- [12] B. Mintz, *Mater. Sci. Technol.* **1996**, 12, 132.
- [13] E. Scheil, *Zeitschrift für Metallkunde* **1942**, 34, 70.
- [14] C. Hoflehner, C. Ramskogler, C. Sommitsch, S. Ilie, J. Six, in *ICS 2018, Proc. 7th Int. Congress on Science and Technology of Steelmaking, Venice* **2018**, p. 148.
- [15] C. Hoflehner, C. Beal, C. Sommitsch, J. Six, S. Ilie, in *28th Int. Conf. on Metallurgy and Materials – Metal*, Brno, Czech Republic **2019**, p. 84.
- [16] M. Lückl, T. Wolcik, E. Povoden-Karadeniz, S. Zamberger, E. Kozeschnik, *Steel Res. Int.* **2017**, 89, 1700342.
- [17] D. Hull, D. J. Bacon, *Introduction to Dislocations*, Oxfordshire: Pergamon Press, Oxford **1984**.
- [18] H. Mecking, U. F. Kocks, *Acta Metall.* **1981**, 29, 1865.
- [19] W. P. Sun, M. Militzer, J. J. Jonas, *Metall. Trans. A* **1992**, 23A, 821.
- [20] W. P. Sun, M. Militzer, J. J. Jonas, *Metall. Trans. A* **1992**, 23A, 3013.
- [21] H. Liu, D. Hu, J. Fu. *Metals* **2019**, 12, 2028.
- [22] H. Badeshia, R. Honeycombe, *Steels: Microstructure and Properties*, 3rd ed., Elsevier, Oxford **2006**.
- [23] D. Loder, S. Michelic, C. Bernhard, *J. Mater. Sci. Res.* **2017**, 6, 24.
- [24] A. Das, S. Das, S. Sivaprasad, M. Tarafder, S. Tarafder, *Proc. Eng.* **2013**, 55, 786.
- [25] G. Avramovic-Cingara, Ch. A. R. Saleh, M. K. Jain, D. S. Wilkinson, *Metall. Mater. Trans. A* **2009**, 40A, 3117.